Robust global detection of forced changes in mean and extreme precipitation despite observational disagreement on the magnitude of change

Iris Elisabeth de Vries[1], Sebastian Sippel[1], Angeline Greene Pendergrass[2,3], and Reto Knutti[1]

[1]Institute for Atmospheric and Climate Science, ETH Zurich, Zurich, Zurich, Switzerland
[2]Earth and Atmospheric Sciences, Cornell University, Ithaca, NY, USA
[3]National Center for Atmospheric Research, Boulder, CO, USA

Correspondence: Iris de Vries (iris.devries@env.ethz.ch)

Abstract. Detection and attribution (D&A) of forced precipitation change is challenging due to internal variability and limited spatial and temporal coverage of observational records. These factors result in a low signal-to-noise ratio of potential regional and even global trends. Here, we use a statistical method – ridge regression – to create physically interpretable fingerprints for detection of forced changes in mean and extreme precipitation with a high signal-to-noise ratio. The fingerprints are constructed using CMIP6 multi-model output masked to match coverage of three gridded precipitation observational datasets – GHCNDEX, HadEX3, and GPCC –, and are then applied to these observational datasets to assess the degree of forced change detectable in the real-world climate.

We show that the signature of forced change is detected in all three observational datasets for global metrics of mean and extreme precipitation. Forced changes are still detectable from changes in the spatial patterns of precipitation even if the global mean trend is removed from the data. This shows detection of forced change in mean and extreme precipitation beyond a global mean trend, and increases confidence in the detection method's power, as well as in climate models' ability to capture the relevant processes that contribute to large-scale patterns of change.

We also find, however, that detectability depends on the observational dataset used. Not only coverage differences but also observational uncertainty contribute to dataset disagreement, exemplified by times of emergence of forced change from internal variability ranging from 1998 to 2004 among datasets. Furthermore, different choices for the period over which the forced trend is computed result in different levels of agreement between observations and model projections. These sensitivities may explain apparent contradictions in recent studies on whether models under- or overestimate the observed forced increase in mean and extreme precipitation. Lastly, the detection fingerprints are found to rely primarily on the signal in the extratropical Northern Hemisphere, which is at least partly due to observational coverage, but potentially also due to the presence of a more robust signal in the Northern Hemisphere in general.

1 Introduction

Precipitation changes may be among the most important consequences of anthropogenic climate change. Yet, robust detection
25 and attribution (D&A) of forced change in the water cycle is impaired by low signal-to-noise ratios. The concept of detection
and attribution is to use climate model simulations in which the applied forcings are known and noise can be reduced by
averaging multiple realisations, to estimate a so-called fingerprint that represents the effect of the applied forcings on climate
variables of interest. Subsequently, the degree to which this fingerprint can be detected in observations is assessed; if the
fingerprint signal is significant and in agreement with the models, the forcing signal is said to be detected and attributed to the
30 applied forcings. The low signal-to-noise ratios of precipitation D&A result from many factors (Balan Sarojini et al., 2016).
First, internal variability of precipitation and related processes is high (Deser et al., 2012; Hoerling et al., 2010; Balan Sarojini
et al., 2012). Second, models show relatively large disagreement in water cycle simulations due to e.g. structural uncertainties
such as parametrised convection, and differing climate and hydrological sensitivities (Pendergrass, 2020). Therefore, models
also show discrepancies with respect to observations (Mehran et al., 2014; Wehner et al., 2020). Lastly, signal robustness
35 suffers from limited spatial and temporal coverage of observations, and biases can be introduced by changing coverage and
station density over time, as well as gridding procedures (Balan Sarojini et al., 2012; Dunn et al., 2020). Here we present a
detection method based on regularised linear regression that is suitable to detect forced changes in global metrics of mean and
extreme precipitation with high signal-to-noise ratio, despite the listed challenges.

Models and observations roughly agree on a rate of specific humidity increase with global mean temperature (GMT) of
40 ≈7%K^{-1}, following theoretical relationships (Held and Soden, 2006; Dai, 01 Aug. 2006). Extreme precipitation scales ap-
proximately with this rate of increased precipitable water and increases over most of the global land, albeit atmospheric dy-
namics modulate the increase in some regions (O'Gorman and Schneider, 2009; Fischer and Knutti, 2016; Pfahl et al., 2017).
Changes in global mean precipitation are associated with the atmospheric energy balance, resulting in a smaller increase of
≈1-3%K^{-1}, with an underlying spatial pattern of hydrological cycle intensification (Allen and Ingram, 2002; Allan et al.,
45 2014; Pendergrass and Hartmann, 2014; Douville et al., 2021). Changes in mean precipitation over land are not well described
by this pattern intensification, though, and are expected to be lower and more complex due to effects of water availability and
relatively higher warming rates over land compared to oceans (Douville et al., 2021; Byrne and O'Gorman, 2015; Roderick
et al., 2014). Besides local climatology, changes in factors such as large-scale atmospheric circulation, water availability and
the vertical structure of the atmosphere play a role in the local precipitation response to forcing (Byrne and O'Gorman, 2015;
50 O'Gorman and Schneider, 2009; Pfahl et al., 2017).

For mean precipitation, anthropogenically forced changes have been detected and attributed on a global land level and for
regions defined by latitude bands (Fischer and Knutti, 2014; Knutson and Zeng, 2018; Noake et al., 2012; Marvel and Bonfils,
2013). Anthropogenic aerosols and GHGs have opposing influences on on the hydrological cycle (Wu et al., 2013; Bonfils et al.,
2020), implying that continued increase of GHGs and decrease of aerosol emissions will lead to stronger GHG signatures in
55 mean precipitation. Although studies agree on the presence of a signal in observations, they disagree on the strength. Models

have been suggested to overestimate (Fischer and Knutti, 2014) as well as underestimate them (Noake et al., 2012; Wu et al., 2013) observed trends.

For extreme precipitation, optimal fingerprinting methods and spatial aggregation approaches have led to detection and attribution of anthropogenically forced changes over global land and for distinct Northern Hemispheric regions (e.g. Min et al., 2011; Zhang et al., 2013; Fischer and Knutti, 2014; Paik et al., 2020; Kirchmeier-Young and Zhang, 2020; Sun et al., 2022). However, for extreme precipitation there is also disagreement regarding the strength of the forced signal in observations. A subset of studies finds CMIP multi-model ensembles generally underestimate changes compared to observations (Min et al., 2011; Fischer and Knutti, 2014; Borodina et al., 2017), whereas others find the opposite (Zhang et al., 2013; Paik et al., 2020; Sun et al., 2022).

Hence, the degree to which model simulations accurately represent the responses of precipitation relevant processes to forcing, and thus accurately simulate past and future changes in precipitation remains up for debate. Knowledge of the severity of current climate change effects on the water cycle, as well as the congruence of modelled and observed historical forced changes in the water cycle is important for adaptation policies and improvement of future projections.

Recent studies using data-science methods of varying complexity for the purpose of reducing the signal-obscuring effects of uncertainties and internal variability have detected forced signals in temperature as well as mean and extreme precipitation (Sippel et al., 2020; Barnes et al., 2019, 2020; Madakumbura et al., 2021). Here, we show that regularised linear regression can construct high signal-to-noise ratio fingerprints of the forced response in mean and extreme precipitation, reducing the influence of internal variability and structural model error on the results. We generate fingerprints for detection and apply these to several station-based observational datasets to assess whether significant forced changes are detected and have emerged from internal variability, and how modelled and observed forced changes compare. We analyse forced signals in annual precipitation anomalies, and also in anomalies from which the global mean trend is removed, relying on spatial pattern information alone. The latter approach highlights relative regional responses to forcing, and tests whether spatial pattern changes in models are in accordance with observations.

2   Methodology

In our detection procedure ridge regression (RR) models are trained on simulated spatial patterns of precipitation with known forcings to determine fingerprints of the modelled forced response (FR) of annual mean total precipitation (PRCPTOT) and annual extreme precipitation (Rx1d: precipitation accumulation on the day with most precipitation each year). The fingerprints are such that they predict the FR from the spatial locations where observational data are available. The RR-fingerprints are applied to observations to isolate an estimate of the real-world FR from internal variability. Several data processing and regression steps are needed to achieve this. We describe the general procedures here; supplementary Sect. S1 contains additional details.

2.1 Model simulations and observational data

The used model simulations come from thirteen CMIP6 models with at least three members with historical and SSP245 data
(Eyring et al., 2016). For models that have more than three of such members, the first three are selected. As unforced control
90   data, 450-year piControl simulations for ten out of the thirteen models are available and used, i.e. 4500 years of unforced data.
See table S1 in the supplement for an overview of CMIP6 data used.

In an effort to address observational uncertainty, three observational datasets are used: for Rx1d HadEX3 (Dunn et al., 2020)
($1.875° \times 1.25°$, 1951-2018), and GHCNDEX (Donat et al., 2013) ($2.5° \times 2.5°$, 1951-2020) are used. For PRCPTOT, HadEX3,
GHCNDEX and GPCC (Schneider et al., 2017) ($2.5° \times 2.5°$, 1951-2019) are used. GPCC does not provide extreme indices and
95   is therefore only used for PRCPTOT. All three observational datasets are gridded data derived from station observations (Dunn
et al., 2020; Donat et al., 2013; Schneider et al., 2017). HadEX3 and GHCNDEX only provide values for gridcells where three
stations are available within the decorrelation length scale of the gridding procedure, leading to spatially incomplete maps.
GPCC, on the other hand, interpolates to all land gridcells. In order to create a reliable GPCC record comparable to the other
datasets, we mask this data to include only gridcells in which data from three stations were available, as per the station density
100   data provided in GPCC as well.

For each timestep within each dataset, coverage differs. In order to generate time-independent fingerprints, we create one
single coverage mask for each dataset representative of 1951-present. Gridcells for which a maximum of 3 time steps (years)
is missing are included, the missing time steps are set to the time mean of the gridcell in question. This implies that the total
fraction of filled-in datapoints (gridcells×timesteps) ranges from 0.4-0.9 %.

105   We note that the nature of model and observational gridded data differs, as model precipitation values are spatial gridcell
averages whereas methods to grid station-based point observations onto a regular grid result in values representative of gridcell
centres (Dunn et al., 2020). This can affect precipitation (extreme) indices in particular, and may reduce the direct comparability
of model and observational absolute values (Dunn et al., 2020; Avila et al., 2015). Trend biases due to this structural difference
have been shown to be negligible, however, justifying the comparison between models and observations made in this study
110   (Avila et al., 2015).

2.2 Data processing

Rx1d is determined as the maximum daily amount of precipitation per year for each location on the original grid. We regrid
modelled PRCPTOT and Rx1d fields onto the grids of HadEX3 and GHCNDEX. As the GPCC grid is nearly identical to the
GHCNDEX grid, we regrid GPCC to the GHCNDEX grid so that the GHCNDEX-regridded CMIP6 simulations can be used.
115   PRCPTOT and Rx1d annual anomalies w.r.t. the 1951-2014 reference period are determined per gridcell. For CMIP6 data,
anomalies of individual members are computed w.r.t. the annual mean of the ensemble mean of the model in question. For
these ensemble means, all available model members are used to reduce noise where possible, even though only three members
are used in the RR model training. This removes potential systematic model biases in absolute precipitation levels, which is
required for meaningful prediction of forced trends.

120   These fields of single-model ensemble member anomalies, masked to observational coverage, serve as predictors to train the RR model, with the goal of predicting the FR, and are used as RR inputs to obtain model FR estimates (FREs). The observational anomalies serve as input to the trained RR model to determine the observed FRE. In a second application of the method, we subtract the masked, area-weighted spatial mean from the predictors and observational data for each time step. These detrended predictors thus only contain the *relative* pattern changes in precipitation.

125   The RR model's purpose is to predict the forced response (FR) from predictors (anomaly maps), hence the RR model is trained with a FR proxy as target variable (predictand). Different RR models are trained for PRCPTOT and Rx1d – each has their own FR proxy as target variable. In order to include the pattern of change, the main FR metric used in this study is based on empirical orthogonal function (EOF) analysis of the unmasked multi-model mean anomaly maps, conceptually similar to a traditional way of extracting FRs (e.g. Santer et al., 1995; Hegerl et al., 1996). In supplementary Fig. S2 we show a comparison

130   between the EOF-based targets and the multi-model global mean, and Fig. S9 shows that using this multi-model global mean as FR target for detection does not lead to different conclusions. Multi-model mean anomalies are determined by taking the mean of the single-model ensemble means and centring this on the 1951-2014 reference period. By first computing single-model ensemble means, all models contribute equally to the multi-model mean regardless of ensemble size. The first EOF of the data represents the spatial pattern that explains most of the variance in the data, and its corresponding first principal component (PC)

135   is a timeseries reflecting the strength of that pattern in the data. We perform the EOF analysis over the entire length (1850-2100) of the multi-model mean record. Given that the response to external GHG forcing is much larger in amplitude than internal variability, the first EOF can be assumed to reflect GHG-caused variance (Hegerl et al., 1996). The PC corresponding to this first EOF is therefore set to be the multi-model forced response best estimate. Each model's ensemble mean data is projected onto the first EOF of the multi-model mean to obtain model-specific FRs, which form the targets for RR training. The model-

140   specific FRs correlate highly with each model's area-weighted global mean change; the average Pearson correlation coefficient is 0.9 for PRCPTOT, and 0.99 for Rx1d. EOF patterns and model specific targets are shown in supplementary Fig. S1. The EOF-derived targets are relatively noisy, however, smoothing the FR targets with a 21-year LOWESS filter before RR model training yields virtually identical results, indicating that the low frequency components of the targets govern the RR model configurations.

145   ## 2.3 Ridge regression

The detection fingerprint is generated by regressing the FR targets onto the spatiotemporal predictors using ridge regression, referred to as training. The resulting fingerprint is a spatial map of coefficients reflecting the relationship between predictors and FR targets in model simulations. For the RR training procedure, we store the predictors in a 2D matrix X of size $n \times p$ (rows $\times$ columns), where each column corresponds to a gridcell in the coverage mask, and the concatenated time series of

150   three members per model make up the rows. The target variable is a vector Y of length n consisting of a concatenation of the targets matching the predictors, i.e. the model member predictors predict their "own" model ensemble mean FR target, to retain within-model physical consistency. The output of the RR training procedure is a coefficient vector β of length p such that:

$$Y = X\beta + \beta_0 + \epsilon \tag{1}$$

Effectively, β – the fingerprint – consists of coefficients for each gridcell in the coverage mask. Applying β to model output
155   (X_{mod}) or observational data (X_{obs}) then gives:

$$\hat{Y}_{mod} = X_{mod}\beta + \beta_0 \tag{2}$$

$$\hat{Y}_{obs} = X_{obs}\beta + \beta_0 \tag{3}$$

in which $\hat{Y}_{mod}$ and $\hat{Y}_{obs}$ are statistical predictions of the modelled and observed FR; referred to as forced response estimates
(FRE). In order to assess whether the external forcing has an effect that is distinct from internal variability, the fingerprint is
160   applied to piControl model simulations to generate an unforced control FRE; $\hat{Y}_{mod,pi}$. All piControl data (4500 years) are input
into the RR model to have a control distribution as large as possible.

β is obtained numerically in R using the package glmnet for k-fold cross-validated ridge regression (Friedman et al., 2010;
Simon et al., 2011). To determine β, the sum of squared residuals plus the sum of squared coefficients times a parameter λ is
minimised (see equation 4 for the objective function). The regularisation parameter λ can be tuned: the higher λ, the stronger
165   the regularisation. This regularisation is the key characteristic of ridge regression.

$$\arg\min \sum (Y_i - \beta X_i)^2 + \lambda \sum \beta^2 \tag{4}$$

The RR cost function is minimised for a set of λs through k-fold cross-validation, in which each fold contains data from
one model. The simultaneous training and cross-validation on all models ensures that the resulting RR-fingerprint generalises
well across models, reflecting where they agree and avoiding overfitting to any particular model. Training on many climate
170   realisations ensures that the resulting RR-fingerprint leads to FREs that are robust to internal variability. This means higher
coefficients are given to gridcells where internal variability is smaller relative to the long-term trend, reflecting where signal-to-
noise ratios and thus predictive value for the FREs are higher. For a more detailed description of RR with glmnet, see (Friedman
et al., 2010; Simon et al., 2011; Sippel et al., 2020).

Regularisation is used since the high number of predictors may otherwise lead to overfitting and unphysical coefficient
175   fingerprints in which e.g. high positive coefficients are offset with adjacent negative coefficients. Regularisation acts to reduce
overfitting, and results in a more homogeneous and smoother fingerprint, which more closely resembles the spatial scales of
precipitation change patterns. It also increases generalisability of the fingerprint, and thus improves performance when applied
to data that have not been seen in the training, such as observations.

There is no objective best approach to select the regularisation parameter λ. Smaller λs reduce bias but increase variance
180   (overfitting) whereas larger λs do the opposite (Friedman et al., 2010; Simon et al., 2011). There are several common options
for λ selection, as default we use λ_{sel}, of which the definition and selection procedure are described in supplementary Sect. S1.

We reason that the most regularised RR model with good performance is a good choice for the detection model, since model performance is very similar within the range of common λs, whereas fingerprint interpretability decreases for λs on the low end of the range. Sensitivities to λ selection are addressed in Sect. 3.4.

185   Note that all the model simulations we use serves as input for RR training - i.e. the model FREs shown in Sect. 3 are not out-of-sample application. Since the purpose of the RR model is to estimate the observed FR from observational data that was not used in training, no independent model data sample for model FR estimation is needed. Figure S3 in the supplement shows that pre-cross-validation results of the RR model applied to out-of-fold data are nearly identical to results of the final cross-validated model.

2.4   Forced trends and signal time of emergence

190

To assess the strength of the observed FREs, we compare linear trends in $\hat{Y}_{obs}$ for the different observational datasets to linear trends in the multi-model FR best estimate Y, as well as to the range of unforced trends given by the piControl FREs $\hat{Y}_{pi}$. In this study, we consider forced change to be detected if $\hat{Y}_{obs}$ trend magnitudes lie outside the 95% confidence interval of trends from control simulations ($\hat{Y}_{pi}$). The magnitude of the observed FRE $\hat{Y}_{obs}$ trends relative to the multi-model FR best estimate 195 Y trends indicates whether CMIP6 models over- or underestimate the real-world forced signals in PRCPTOT and Rx1d.

Besides linear trends, we also assess the signal-to-noise ratio (SNR) of the observed FREs. We define SNR based on Hawkins et al. (2020), but we note that the signals here are global, as opposed to local signals in Hawkins et al. (2020). In order to separate the signal from the noise in FREs, FREs are related to a smoothed, long-term forcing proxy as a covariate. Since global precipitation change scales with global temperature change, as described in the introduction, the long term trend in 200   precipitation FREs can be isolated using the long term trend in global temperature (see supplementary Fig. S4). Hence, the signal S is defined as the observed FRE regressed onto smoothed global mean surface temperature (GMST) from Cowtan and Way (2014). GMST is smoothed with a 21-year LOWESS-filter to remove interannual variability while keeping the long term trend. The noise N is defined as the standard deviation (σ) of the residuals of this linear fit, i.e. $\sigma(\hat{Y}_{obs} - S)$. The SNR ($\frac{S}{N}$) thus relates the observed FRE signal to observed FRE noise, providing a measure of signal emergence. The mean signal is 205   centred to zero in the 21-year period 1951-1971, as we see minimal measurable forcing effects in precipitation metrics up to then. Between the 1951-1971 period and the present, the signal and thus the SNR increases. This allows us to determine the time of emergence (ToE) of a forced climate signal in mean and extreme precipitation, defined as the year after which the SNR consistently remains higher than 2.

3 Discussion of results

3.1 Context: Precipitation change in model simulations and observations

In order to put the detection results in context, we first assess the general characteristics of historical precipitation trends
in models and observations. Figure 1 shows maps of annual linear trends for PRCPTOT and Rx1d from the CMIP6 ssp245
multi-model mean and the observational datasets over the 1951-2014 period.

For PRCPTOT (left panel) the model trend map (Fig. 1a) shows the well-established mean precipitation forced change
spatial pattern, including a net global increase and an intensification of the global water cycle pattern (Douville et al., 2021).
All observational datasets (figures 1c, e and g) contain features that resemble the multi-model mean forced patterns such as
wettening in high latitudes. There are also some regions, such as Southeast Asia and West Africa, where observed and simulated
trends have opposite signs. Uncertainties in the net precipitation response to the opposing forcing effects of greenhouse gases
and aerosols in the second half of the 20th century, as well as internal variability, likely play a role in these discrepancies
(Bonfils et al., 2020). The different observational datasets generally agree with one another, but a stronger trend over western
North America in GHCNDEX (Fig. 1e) stands out. For HadEX3, GHCNDEX, and GPCC, models and observations agree on
the sign of the PRCPTOT trend for 74%, 85%, and 68% of gridcells. For Rx1d (right panel) model trends (Fig. 1b) also reflect
well-known changes, which are predominantly positive, especially over land. Observational records (figures 1d and 1f) agree
in that they also feature mostly positive trends. For HadEX3 and GHCNDEX, models and observations agree on the sign of
the Rx1d trend for 71% and 75% of gridcells. The fact that simulated trend patterns appear smoother and smaller in magnitude
than observational trend patterns is primarily due to multi-model mean averaging.

The first EOFs underlying the RR targets look virtually identical to the simulated trend patterns, which implies that the first
EOFs capture the forced trend signals (see supplementary Fig. S1).

3.2 Detection fingerprints and observed FRE

Figure 2 shows the detection fingerprints, FREs and forced trends for models and observations obtained with RR.

The top panel of Fig. 2 shows the regression coefficient fingerprints that best predict the FR while minimising variance
due to internal variability and model disagreement, as described in Sect. 2. Only the fingerprint on the HadEX3-mask is
shown here, GHCNDEX-masked and GPCC-masked fingerprints feature similar patterns where coverage overlaps, as shown
in supplementary Fig. S5, increasing confidence in the generated RR-patterns and the method.

For both PRCPTOT (2a) and Rx1d (2b), large coefficients indicate changes with a high SNR and a time evolution that
corresponds to the global FR time evolution. Positive coefficients indicate changes with the same sign as the global FR,
whereas negative coefficients indicate changes with opposite sign. RR tends to rely on regions with smaller but more robust
changes for FR prediction, whereas some regions with larger changes such as the tropics contribute less to the prediction,
due to their high internal variability and uncertainty (Kent et al., 2015). Regions with very small coefficients coincide with
where CMIP6 models have been shown to disagree strongly on the sign of change, e.g. the location of the transition from
negative (south) to positive (north) coefficients in Europe for PRCPTOT, and central America and the whole of Australia for
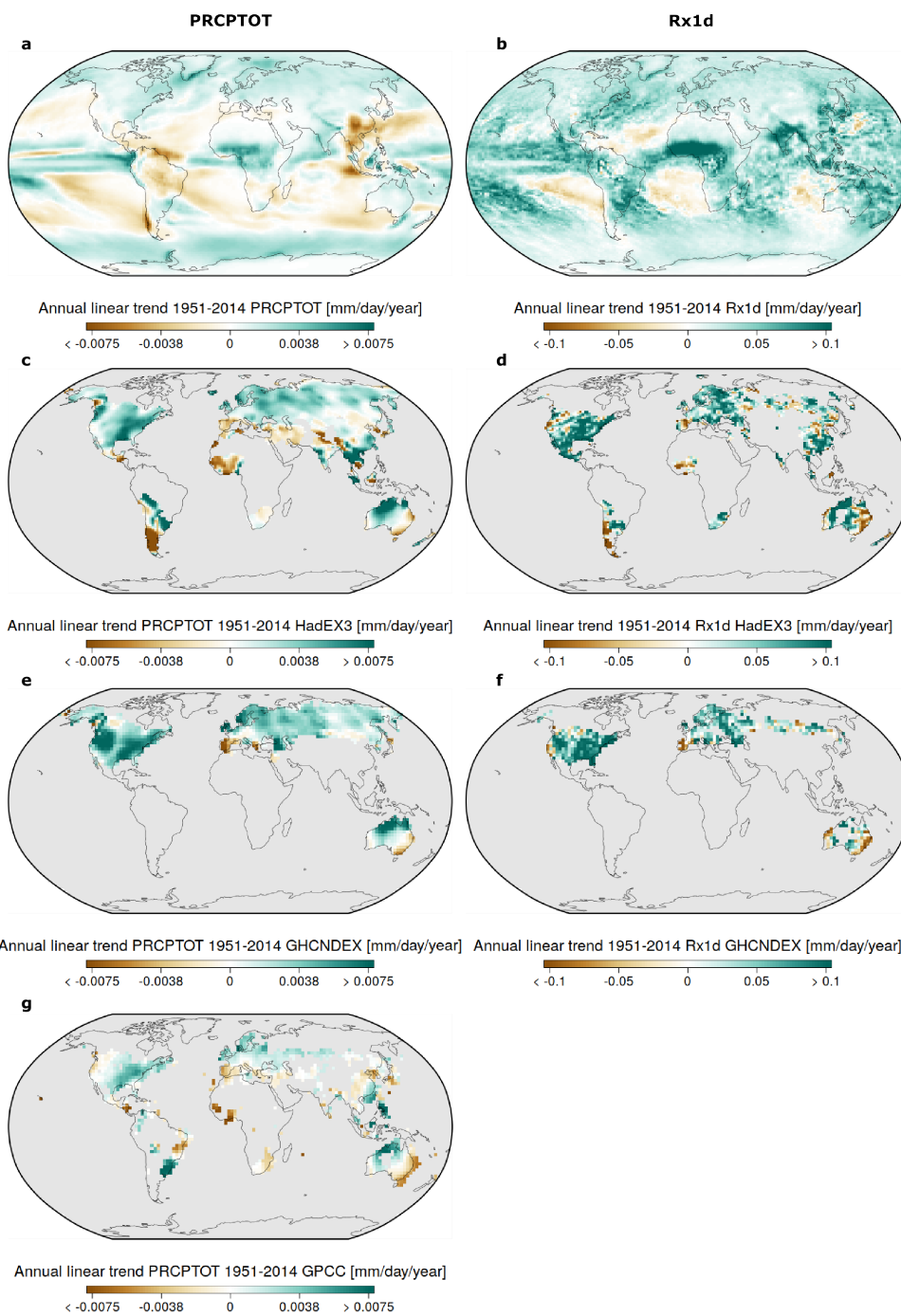
Figure 1. Mean total precipitation (PRCPTOT, left) and extreme precipitation (Rx1d, right) 1951-2014 annual linear trends in the CMIP6 multi-model mean (a, b); in HadEX3 observational data (c, d); in GHCNDEX observational data (e, f); and in GPCC observational data (g).
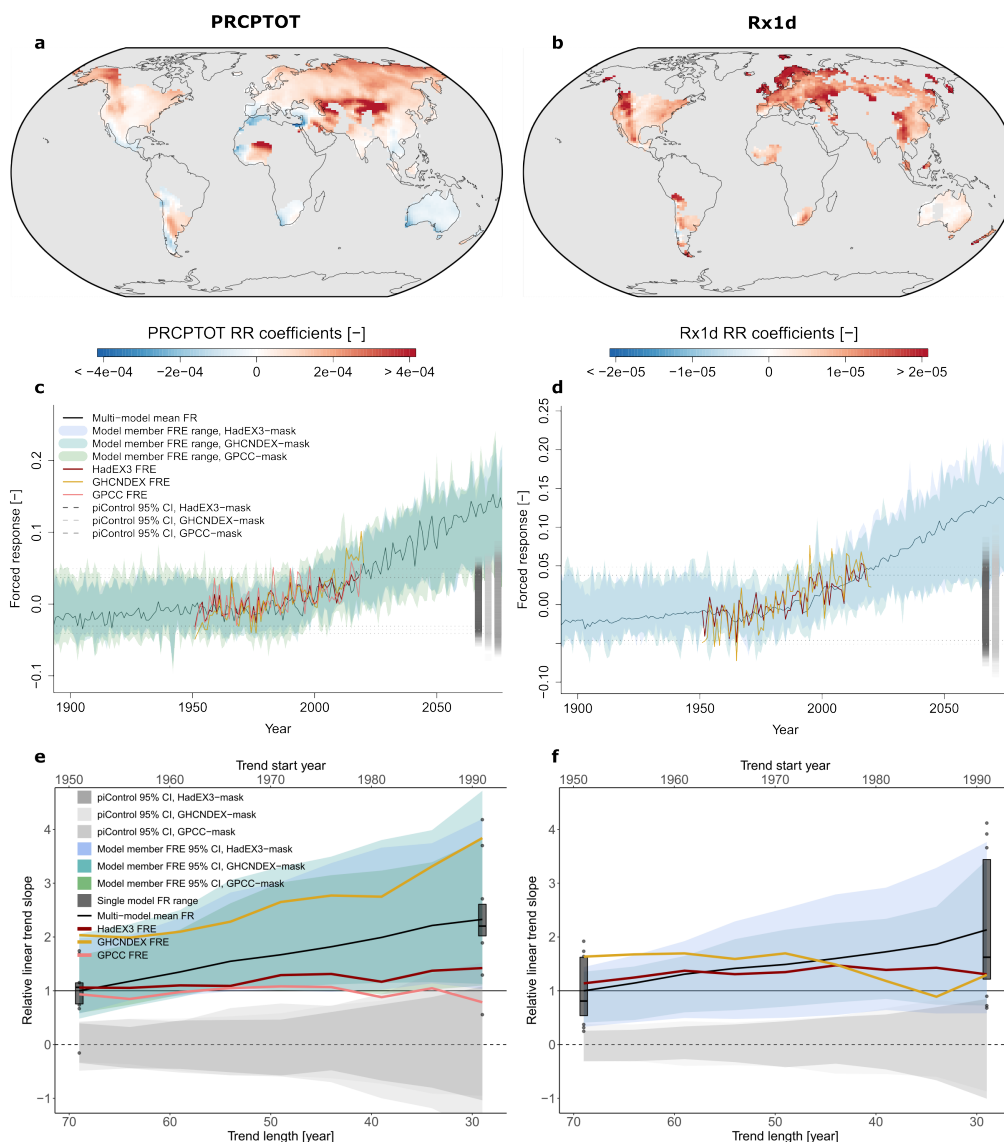
Figure 2. Annual mean total precipitation (PRCPTOT) and extreme precipitation (Rx1d) ridge regression detection fingerprints for HadEX3 coverage (top), corresponding forced response estimates (FREs) (middle), and linear FRE trends as a function of trend period (bottom). In (c) and (d), black lines represent the multi-model forced response (FR) best estimate, coloured shading the full range of model FREs, coloured lines the observed FRE, grey dashed lines the unforced internal variability of the FR pattern (piControl FRE 95% confidence interval (CI)). In (e) and (f), black lines represent the multi-model FR best estimate trend, coloured shading the 95% confidence interval of model FRE trends, coloured lines the observed FRE trends, grey shading the piControl trends, black boxplots the model ensemble mean target trends. Trends are computed from a variable start year until the end year of the observational time series (2018 for HadEX3, 2019 for GPCC, 2020 for GHCNDEX, 2018 for multi-model FR best estimate and model ensemble mean trend). Start years vary between 1951 and 1991 with increments of 5. piControl trends are computed over periods equally long as the corresponding forced trends. All linear trends are normalised with respect to the multi-model FR best estimate 1951-2018 trend, i.e. the leftmost point on the black line.

both PRCPTOT and Rx1d (Douville et al., 2021; Giorgi et al., 2014; Westra et al., 2013; Sun et al., 2022; Kotz et al., 2022; Kent et al., 2015). For many of these regions, the disagreement among models about precipitation change can be traced back to the influence of circulation changes on precipitation changes, which are particularly uncertain; for example, expansion of
245 subtropical dry zones.

Several specific features that reflect the FR pattern of PRCPTOT and Rx1d can be distinguished in the fingerprints. The PRCPTOT fingerprint features negative coefficients in southern Europe and northern Africa, as well as South-Africa and Australia, which reflect the drying pattern corresponding to expected forced change in the hydrological cycle (Douville et al., 2021). Additionally, the climatologically wet Pacific Northwest exhibits positive coefficients as the air that rains out due to
250 orographic lift by the Cascade, Coastal, and Olympic mountain ranges becomes increasingly moist with climate change. The rain shadow on the lee side features negative coefficients. The Rx1d fingerprint looks more homogeneously positive than for PRCPTOT, reflecting the expectation of a positive trend in Rx1d over almost all land regions, as seen in Fig. 1 (Pfahl et al., 2017). The strong positive coefficients in Northern Europe and the North-American West Coast can likely be explained by the systematic nature of extreme precipitation in these regions – wet ocean westerlies making landfall –, which results in a
255 consistent response to increased atmospheric moisture and thus high predictive value for the global FR (Pfahl and Wernli, 2012). The smaller positive or even negative coefficients in the tips of South America and South-Africa correspond to regions where dynamical changes are known to mask thermodynamic increases in Rx1d (Pfahl et al., 2017; Kotz et al., 2022; Li et al., 2021).

The similarities in the maps for PRCPTOT and Rx1d indicate that the signs of change in PRCPTOT and Rx1d correspond
260 in most regions, pointing towards a precipitation distribution shift to higher mean and extreme precipitation levels. As mentioned, however, the magnitude of the increase is larger for Rx1d than for PRCPTOT, and regions where negative changes in PRCPTOT exist in combination with positive changes in Rx1d are also found. This corresponds to widening of the precipitation distribution and complies to the expected forced increase in precipitation variability (Zittis et al., 2021; Pendergrass et al., 2017). From an impacts perspective, this could imply that the background climate in some regions dries while wet extremes
265 become more intense, which can increase both drought and flood risks (Tramblay et al., 2019).

The middle panels of Fig. 2 show the FREs for PRCPTOT (2c) and Rx1d (2d), which are the result of applying the RR-fingerprints to model simulations and observational data. The green/blue shading shows the range of FREs from CMIP6 individual member data for all observational masks. The consistency of the trend in the model FRE envelopes and the multi-model FR best estimate (black line) confirms that the RR-fingerprints are indeed suited to capture the global climate change
270 signal in PRCPTOT and Rx1d from spatially incomplete model data. The model FREs show a slight high bias in early years where the target is at the low end of its range, and a slight low bias in late years where the target is at the high end of its range. This effect is expected since the regularisation "trades" some goodness of fit for generalisability, and makes the FRE more conservative.

The coloured lines show FREs from observations. The observed FREs lie well within the model FRE range, exhibit similar
275 variance, and follow the trend of the multi-model FR best estimate. These trends in the observed PRCPTOT and Rx1d FREs indicate that the strength of the forcing pattern increases in observations indeed, and generally agrees with model projections.

The grey dashed lines show the 95% confidence interval of the FRE from unforced piControl data, and the piControl FRE distribution is also shown as a point cloud to the right of the timeseries, reflecting the internal variability range of the detection pattern. Over the historical period, observed FREs have moved from the middle towards the upper bound of the piControl range, and the multi-model FR best estimate and model FREs leave the piControl range still in the first half of the 21st century. All of the above points to the unambiguous detection of forced climate change in annual PRCPTOT and Rx1d in all observational datasets used.

We note that the GHCNDEX FRE for PRCPTOT shows a distinct uptick towards the end of the record, which likely is related to the coverage of GHCNDEX being almost exclusively in the higher Northern latitudes (more so than for the other datasets), which contribute disproportionately in these particular years. However, based on the analysis here, we cannot differentiate whether this is an artefact, internal variability, or indicative of an increasing forced rate of change in PRCPTOT.

Besides visual inspection of FRE timeseries, quantitative detection statements can be made based on the trends in these timeseries. For lack of evidence for a particular FR polynomial, the high amount of noise in observed FREs, and ease of interpretation, linear trends are assumed. The trends in PRCPTOT and Rx1d, however, are not constant with time in the period of interest, so we also include the dependence of forced trend estimates on the length and start year of the trend period. Figures 2e and 2f show a quantitative overview of the linear trends of targets and FREs as a function of start year and trend length. Findings are normalised with respect to the 1951-2018 multi-model FR best estimate trend.

Since forced trends in both PRCPTOT and Rx1d only begin to appear around 1975, the multi-model FR best estimate trends are larger in more recent trend periods that omit earlier years (toward the right side of the x-axis). The model FRE trend 95% confidence intervals (green/blue shading) are reasonably symmetric around the multi-model FR best estimate and include the majority of the ensemble mean target trends (black boxplots). This agreement of model FRE trends with FR target trends shows that the RR-model does well in estimating the forced trend magnitudes. Part of the intermodel spread in both FR targets (boxplots) and model FREs is explained by the different climatological levels of precipitation among models and their different climate sensitivities, and in part by model uncertainties in temperature-independent precipitation adjustments (Fläschner et al., 2016). Despite the large spread, there is only little overlap of the model FRE trend confidence interval and the piControl trend confidence interval (grey shading), implying that almost the entire range of model FRE trends lies outside the range of trends possible in an unforced climate. This confirms once again that there is a robust forced signal in mean and extreme precipitation.

The observed FRE trends for both PRCPTOT and Rx1d (coloured lines) exceed zero, lie within the model FRE trend confidence interval and outside the piControl confidence interval for all trend lengths (apart from GPCC trends over the most recent 40 years or shorter), confirming detection of forced change in observations. Although forced change is unambiguously detected in all datasets, the degree of observed change depends on the observational dataset considered.

GHCNDEX yields higher observed FRE trends than the multi-model FR best estimate trend for PCRPTOT whereas HadEX3 and GPCC yield lower observed forced trends. Hence, GHCNDEX suggests that CMIP6 models *underestimate* the forced change in PRCPTOT, whereas HadEX3 and GPCC suggest CMIP6 models *overestimate* it. The higher trends in GHCNDEX PRCPTOT are partly caused by the few high outliers towards the end of the GHCNDEX timeseries mentioned earlier, but also persist when these are removed from the timeseries.

For Rx1d, GHCNDEX and HadEX3 FREs show more similar trends, although GHCNDEX trends again exceed HadEX3 trends for trends that include years before 1975. For more recent periods, GHCNDEX shows smaller trends than HadEX3. In general, FRE trend increases in both observational datasets flatten out for periods from 1975 to the present, where trends smaller than the multi-model FR best estimate are found. By contrast, periods including years prior to 1975 suggest observed trends larger than in the multi-model FR best estimate.

Whereas the magnitudes of the observed FRE trends differ considerably among the observational datasets in some cases, as highlighted above, the relative trend fluctuations over time resemble each other in all datasets. This increases confidence in the consistency of the method, and suggests that differences in spatial coverage and data operations among observational datasets are the main sources of uncertainty in observed forced trend estimation.

Although these results are sufficient to conclude that the detection of forced change in global mean and extreme precipitation is unequivocal, internal variability and short record length preclude our ability to conclude whether the observed change is weaker or stronger than models suggest. The use of multiple observational datasets and the time-dependent view of the forced trends in observations shows that the magnitude of forced change detected in precipitation observations is sensitive to choices on the specifics of the analysis. In previous studies, opposing conclusions have been drawn as to the magnitude of forced precipitation change in observations relative to model simulations, as noted in the introduction. Our results show that both conclusions can be true, depending on the observational dataset and the forced trend metric used.

Confidence in these results is strengthened by the consistency of the variability in the model FREs and observed FREs. The residuals of the linear fit to the observed and modelled FREs have comparable distributions, shown in supplementary Fig. S6. This residual variance consistency justifies the use of the model-derived RR-fingerprint on observations, and decreases the likelihood of spurious detection. Confidence in the method is also enhanced by its robustness to target metric; the results above also hold when the global mean is used as FR target, as shown in supplementary Fig. S9.

3.3 Detection based on relative spatial patterns of precipitation alone

It is not surprising that forced change in mean and extreme precipitation can be detected on a global scale, given the consensus on global mean increases in PRCPTOT and Rx1d with increasing global temperatures. A more powerful detection statement can potentially be made, however, if forced change can be detected in the spatial pattern of precipitation observations alone, excluding the global mean trend. Therefore we attempt to construct RR-models based on training data from which the global mean trend is removed (detrended) by subtracting the coverage-masked, area-weighted spatial mean for each time step. The resulting fingerprints are then applied to observations which are detrended in the same way.

Figure 3 (top) shows the RR-fingerprints for detrended predictors on the HadEX3 mask for mean and extreme precipitation (GHCNDEX and GPCC masked fingerprints look similar where coverage overlaps, see supplementary Fig. S7). In these fingerprints, negative coefficients indicate a change that is in phase with the FR but of opposite sign, which can point to a decrease, but also to an increase with a smaller slope than the (coverage-masked) global mean increase. The latter is the case when coefficients flip sign from positive in Fig. 2, where the trend is included, to negative in Fig. 3. Positive coefficients in Fig.
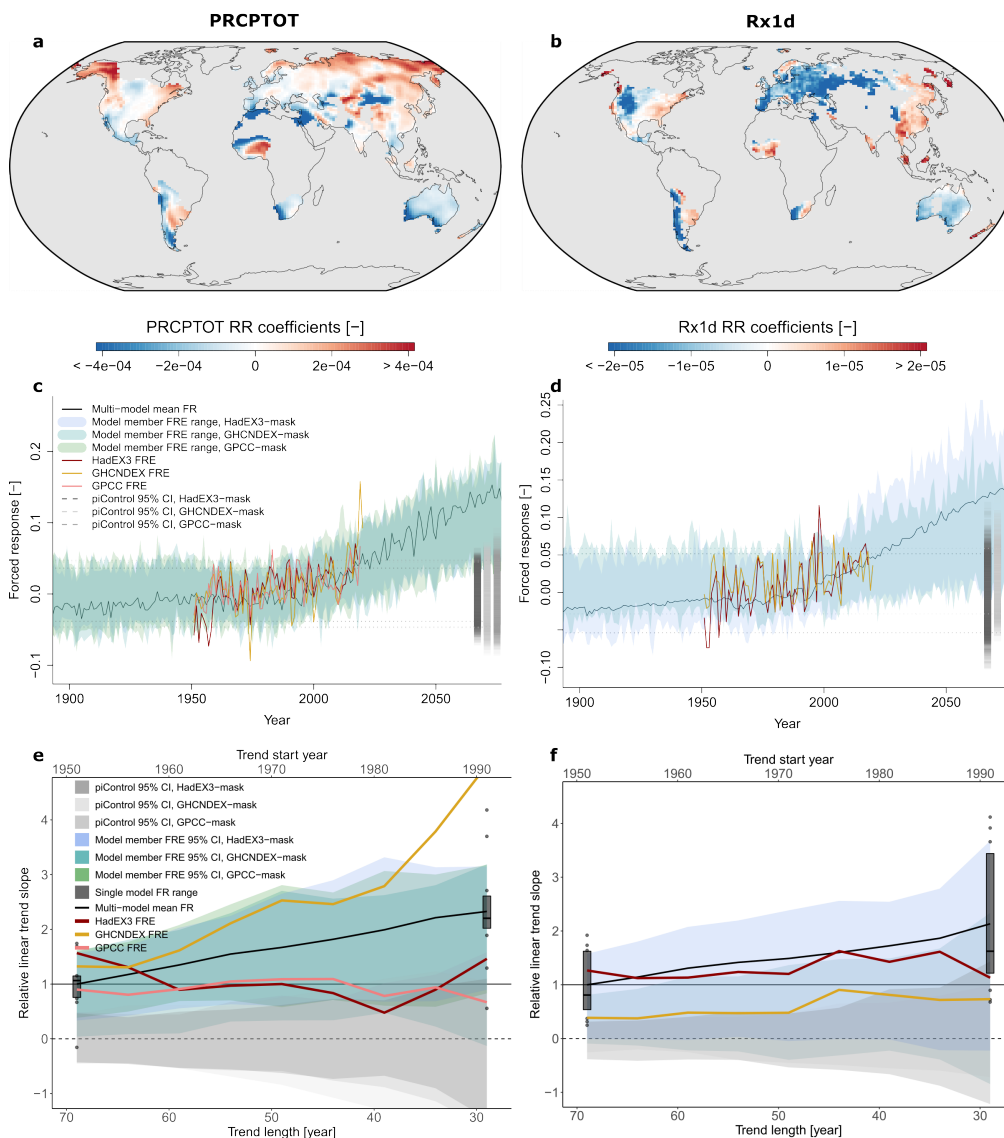
Figure 3. As Fig. 2 but for detrended predictors. Detrending implies removing the masked, area-weighted spatial mean from the model member data and observational data for each time step.

345 3, on the other hand, indicate increases with slopes larger than the global mean increase. As for the fingerprints in Fig. 2, large coefficient magnitudes in Fig. 3 signify high SNR but not necessarily large changes in an absolute sense.

Inspection of the detrended fingerprints leads to several interesting insights. Both for PRCPTOT and Rx1d we see that some regions with large regression coefficients flip sign. As stated above, this reflects high-SNR changes of the same sign but with a smaller rate of change than the global mean. This again shows that RR relies to a large degree on small but consistent changes,

350 e.g. the Tibetan plateau for PRCPTOT. This effect is even more strongly visible in the Rx1d fingerprint, since continental Europe and western North-America – the regions with strong positive coefficients in the fingerprint with global mean included – flip sign. Rx1d increases in these regions are thus smaller than global mean, yet strong indicators of forced change in the context of internal variability and uncertainty among models. Rx1d increases likely are dominated by large tropical rainfall increases, as indicated by persistent positive coefficients in tropical regions and the North-American and Asian east coasts.

355 For both PRCPTOT and Rx1d, the regions of primary importance largely remain the same between the two fingerprint types. This implies that the fingerprint with the global mean trend included picks up on high SNR forced signals beyond the large scale mean increase.

The observed FREs for detrended PRCPTOT and Rx1d (coloured lines) in figures 3c and 3d show a clear positive trend that is in agreement with the multi-model FR best estimate (black line). Recall that the FREs in figures 3c and 3d are derived from
360 observations from which the global mean is removed, meaning that the relative spatial patterns of PRCPTOT and Rx1d alone exhibit a clearly detectable forced long term trend. However, the larger spread in the observed FREs compared to figures 2c and 2d shows that detrending of the predictors – i.e. removing part of the signal – results in larger variability of the observed FREs, which reduces the SNR ratio of the trends.

The model FREs also exhibit larger variability, which causes the forced and piControl trend confidence intervals (green/blue
365 and beige/gray) to overlap more (figures 3e and 3f), indicating a lower detectability of forced change in detrended model data. Particularly for GHCNDEX-masked Rx1d data (green shading in Fig. 3f), the low coverage in combination with detrending removes so much information that FR estimation from model data is substantially impaired. With weaker regularisation the forced trend still cannot be estimated from detrended GHCNDEX data.

Despite the reduced information given to the RR-model in the detrended case, figures 3e and 3f show that forced change
370 is still detected using the spatial pattern alone. The observed forced trends lie outside the piControl confidence interval and are in reasonable agreement with the multi-model FR best estimate trends for longer trend lengths. For shorter trend lengths, the higher variability in the FREs leads to higher trend variability as well. Consistent with figures 2e and 2f, we see that HadEX3 and GPCC show smaller PRCPTOT trends than the multi-model FR best estimate, whereas GHCNDEX shows larger trends. We note that very high GHCNDEX PRCPTOT FRE trends seen here are untrustworthy given that GHCNDEX residual
375 consistency in the detrended setup is insufficient (see supplementary Fig. S8). HadEX3 Rx1d trends agree very well with the multi-model FR best estimate trends.

A possible interpretation of the forced change detection in HadEX3 Rx1d but lack thereof in GHCNDEX Rx1d, is that the FR in Rx1d can be detected in absence of the global mean, but that sufficient coverage is necessary. The seemingly higher sensitivity of Rx1d to detrending is likely because the Rx1d FR is more spatially homogeneous, which implies that global mean
380 detrending removes much more of the signal than for the spatially heterogeneous PRCPTOT FR. Taken together, the above shows, first, detection of forced change in mean and extreme precipitation beyond a global mean trend, second, the power of RR for signal extraction from high-dimensional noisy data, and third, the accuracy of the CMIP6 climate models in simulating the processes relevant to the spatial pattern of forced change in mean and extreme precipitation.
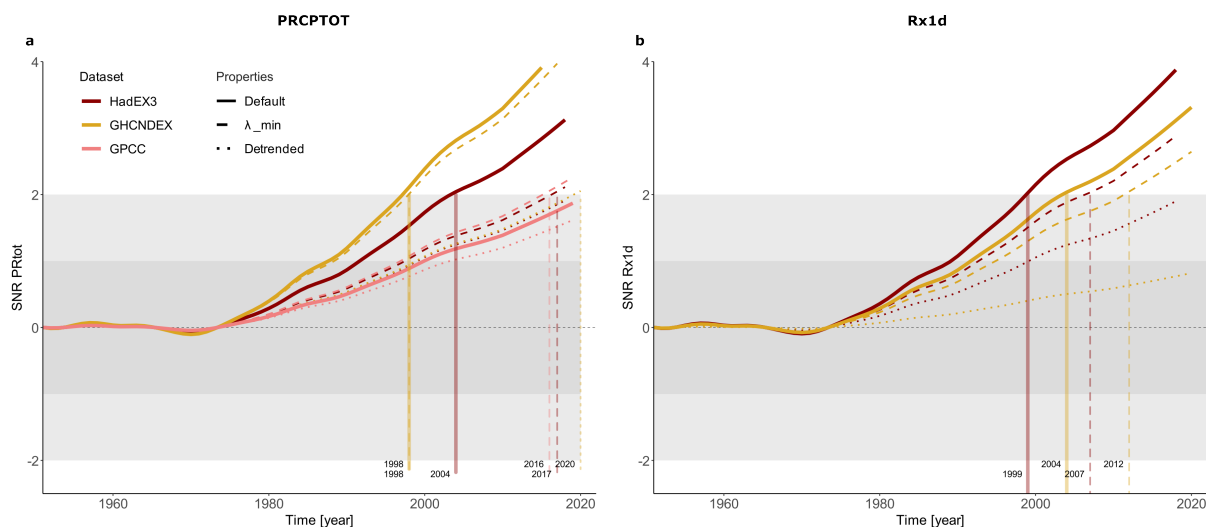
Figure 4. SNRs of mean total precipitation (PRCPTOT) (a) and extreme precipitation (Rx1d) (b) FREs in GHCNDEX, HadEX3 and GPCC, including senstivies to regularisation parameter (dashed) and global mean detrending (dotted). Exceedance of an SNR of 2 implies emergence. Signal is defined as FRE regressed onto 21-year LOWESS filtered GMST, noise as residuals of this fit.

3.4 Time of emergence

385   The FREs and trends in figures 2 and 3 provide evidence that the observed forced trends are larger than the unforced piControl trend distribution, both with and without global mean signal. Figure 4 provides the SNR as a quantitative assessment of the observed FRE signal strength relative to the observed FRE variability, as defined in Sect. 2.4. Besides the default case (solid lines, corresponding to the FREs in figures 2c and 2d), the detrended SNR (dotted, corresponding to the FREs in figures 3c and 3d) as well as the SNR for less regularised RR-models with minimal cross-validated mean squared error (λ_{min}) (dashed) are

390   shown (Friedman et al., 2010; Simon et al., 2011).

Time of emergence (ToE) – the time after which the SNR consistently is higher than 2 – is indicated by the vertical lines. We consider the ToE definition above a consistent measure of effective SNR in the real climate, since both signal and noise are derived from observations. To assess the effects of possible autocorrelation within observational residuals as well as possible biases due to the relatively small sample size, we also compute SNRs w.r.t. a noise measure derived from FREs of control

395   simulations, as in Hawkins and Sutton (2012) This definition of SNR results in similar outcomes (not shown).

Overall, figures 4a and 4b show emergence of forced change within four years of 2000 in both PRCPTOT and Rx1d in GHC-NDEX and HadEX3 for the default setup (solid lines). The nearly identical ToE for PRCPTOT and Rx1d obtained using our method of FR estimation is noteworthy, given earlier suggestions of a later emergence of PRCPTOT due to higher uncertainties and internal variability (Fischer et al., 2014). The exact ToE differs between datasets, as expected given the different trends seen in Fig. 2, and GPCC PRCPTOT does not show emergence at all due to its weaker trend combined with high variability.

400   We note that GPCC is constructed using a different gridding procedure than HadEX3 and GHCNDEX, and also our handling

of GPCC is different due to the need to speficy a coverage mask based on station density, whereas HadEX3 and GHCNDEX provide their own coverage masks. Interestingly, Rx1d ToE is earlier in HadEX3, despite larger long-term linear trends in GHCNDEX. This reflects the higher efficiency of RR in reducing variance while capturing the signal for the higher spatial coverage of HadEX3.

The benefit of regularisation becomes evident when comparing the default case to the λ_{min} setup, where regularisation is such that the training cross validation error is smallest (see supplementary Sect. S1.3 for a more extensive definition). For λ_{min} FREs, SNR is lower and ToE is later (despite slightly larger FRE trends), due to the increased variance in the λ_{min} FREs caused by overfitting on the training data. For GPCC this effect is not seen, since the regularisation for GPCC in the default case is weak, i.e. λ_{sel} and λ_{min} are not far apart and variance in the FRE hardly increases for λ_{min}.

Lastly, the effect of removing the global mean from the data (detrended), discussed in the previous section, is shown in the dotted lines. Due to the increased variance in the FREs, SNRs decrease and ToEs increase. Yet, signals have emerged or are close to emergence in all detrended cases except for GHCNDEX Rx1d, once again confirming the detection of forced climate change in spatial patterns of PRCPTOT and Rx1d.

All of the above points to detection and emergence of a forced response in observations of mean and extreme precipitation, robustness of the detection method, and representation accuracy of forced and internal variability patterns of precipitation in climate models.

4   Conclusions and outlook

We demonstrated the detection and emergence of forced change in mean and extreme precipitation beyond internal variability using a recently-introduced detection method based on regularised linear regression. We generate regression models for detection of forced change based on climate simulations, consisting of physically interpretable fingerprints that optimise signal-to-noise ratio. We detect forced trends in both mean and extreme precipitation that lie outside the piControl confidence interval of unforced variability in three different observational datasets. The unequivocalness of the detection of forced change is further demonstrated by the sustained detection from the spatial pattern of precipitation alone, after subtracting the global mean trend from the data. A similar result was shown earlier for mean precipitation (Barnes et al., 2019), and is extended here to extreme precipitation. This finding also reinforces confidence in the ability of CMIP6 models to respresent processes that govern the (large-scale) spatial distribution of precipitation. Simultaneous emergence of the forced signal from internal variability in both PRCPTOT and Rx1d demonstrates the value of RR-based fingerprint construction for high signal-to-noise ratio estimation of forced responses.

Despite the robustness of the results, the magnitude of forced trends in observations and models depends on the period over which trends are calculated, as well as on the observational dataset. These sensitivities emphasise the difficulty associated with quantitative assessment of observed changes, as demonstrated by apparent contradictions in recent studies on whether models under- or overestimate the observed changes in precipitation. In addition to methodology, model uncertainties, changing

observation station densities, internal variability and structural differences between model simulations and observational data
435   also affect the estimation of the forced response (Noake et al., 2012; Dunn et al., 2020).

It is important to note that the influence of Northern Hemisphere (NH) precipitation is disproportionately strong in this analysis. Part of this larger NH contribution may be due to stronger or earlier emergence of a forced response, which has been found in other studies (King et al., 2015). However, the uneven distribution of measurement stations over the global land plays a large role as well. Therefore, the global detection found in this study may not be representative for smaller sub-regions,
440   especially outside of the NH. Furthermore, preliminary results suggest that detection is sensitive to seasonal process specifics – we find that forced change is not detected in June-July-August (NH summer), on both global and NH specific scales (see supplementary Fig. S12). This is potentially related to the convective nature of precipitation in NH summer. We provide a preliminary application of the method to regional and seasonal scales in supplementary Sect. S3. Extending the approach to D&A of precipitation changes on regional and seasonal spatiotemporal timescales is of great importance to increase practical
445   relevance of the results for risk assessment and adaptation.

In this study we do not explicitly separate the effects of different forcings (GHG, aerosols, natural). We assume, however, that the analysis primarily pertains to GHG-forcing since the RR fingerprint is based on SSP245 projections through 2100, when GHG forcing dominates (Chen et al., 2021). Nonetheless, an extension of the present study explicitly separating different forcings would be insightful to further characterise the effects of different forcing agents in the real climate, and potentially
450   identify sources of disagreement between models and observations. This is important as Wu et al. (2013) shows that different models may agree on the simulated response to all forcings combined, while they differ greatly on separate responses to GHG and aerosol forcings alone. Correct simulation of the relative effects of different forcing agents is important for scenario development and climate action targets, meaning further investigation of these model discrepancies is imperative. RR-based analyses may enable establishment of observational constraints on the precipitation response to different drivers, which can
455   help constrain projections of near term changes in mean and extreme precipitation.

Code and data availability. All original CMIP6 data used in this study are publicly available on https://esgf-node.llnl.gov/projects/cmip6/. HadEX3 and GHCNDEX data are publicly available on https://www.climdex.org/access/. GPCC data are publicly available on https://opendata.dwd.de/climate_environment/GPCC/html/gpcc_normals_v2020_doi_download.html. Preprocessed data and ridge regression model training code are available on [to be added], additional code is available upon request.

460   *Author contributions.* IEdV: conceptualisation, methodology, software, formal analysis, writing, visualisation. SS: conceptualisation, methodology, software, writing - review & editing, supervision, funding aqcuisition. AGP: conceptualisation, writing - review & editing, supervision, funding aqcuisition. RK: conceptualisation, writing - review & editing, supervision, funding aqcuisition.

Competing interests. The authors declare no competing interests.

Acknowledgements. We thank U. Beyerle, R. Lorenz, and L. Brunner for the preparation and maintenance of CMIP6 data. We acknowledge the World Climate Research Programme's Working Group on Coupled Modelling, which is responsible for CMIP, and we thank the climate modeling groups for producing and making available the model output. For CMIP, the U.S. Department of Energy's Program for Climate Model Diagnosis and Intercomparison provides coordinating support and led development of software infrastructure in partnership with the Global Organization for Earth System Science Portals. IEdV and SS acknowledge funding received from the Swiss National Science Foundation within the project "Combining theory with Big Data? The case of uncertainty in prediction of trends in extreme weather and impacts" (grant no. 167215). SS acknowledges funding from the Swiss Data Science Centre within the project "Data Science-informed attribution of changes in the Hydrological cycle" (DASH; C17-01) and within the European Union H2020 project "Artificial intelligence for detection and attribution" (XAIDA; grant no. 101003469). AGP was supported by the U.S. Department of Energy, Office of Science, Office of Biological & Environmental Research (BER), Regional and Global Model Analysis (RGMA) component of the Earth and Environmental System Modeling Program under Award Number DE-SC0022070 and National Science Foundation (NSF) IA 1947282, and by the National Center for Atmospheric Research (NCAR), which is a major facility sponsored by the NSF under Cooperative Agreement No. 1852977.

References

Allan, R. P., Liu, C., Zahn, M., Lavers, D. A., Koukouvagias, E., and Bodas-Salcedo, A.: Physically consistent responses of the global atmospheric hydrological cycle in models and observations, Surveys in Geophysics, 35, 533–552, https://doi.org/10.1007/s10712-012-9213-z, 2014.

480 Allen, M. R. and Ingram, W. J.: Constraints on future changes in climate and the hydrologic cycle, Nature, 419, 228–232, https://doi.org/10.1038/nature01092, 2002.

Avila, F. B., Dong, S., Menang, K. P., Rajczak, J., Renom, M., Donat, M. G., and Alexander, L. V.: Systematic investigation of gridding-related scaling effects on annual statistics of daily temperature and precipitation maxima: A case study for south-east Australia, Weather and Climate Extremes, 9, 6–16, https://doi.org/10.1016/j.wace.2015.06.003, 2015.

485 Balan Sarojini, B., Stott, P. A., Black, E., and Polson, D.: Fingerprints of changes in annual and seasonal precipitation from CMIP5 models over land and ocean, Geophysical Research Letters, 39, https://doi.org/10.1029/2012GL053373, 2012.

Balan Sarojini, B., Stott, P. A., and Black, E.: Detection and attribution of human influence on regional precipitation, Nature Climate Change, 6, 669–675, https://doi.org/10.1038/nclimate2976, 2016.

Barnes, E. A., Hurrell, J. W., Ebert-Uphoff, I., Anderson, C., and Anderson, D.: Viewing forced climate patterns through an AI Lens, 490 Geophysical Research Letters, 46, 13 389–13 398, https://doi.org/10.1029/2019GL084944, 2019.

Barnes, E. A., Toms, B., Hurrell, J. W., Ebert-Uphoff, I., Anderson, C., and Anderson, D.: Indicator Patterns of Forced Change Learned by an Artificial Neural Network, Journal of Advances in Modeling Earth Systems, 12, e2020MS002 195, https://doi.org/10.1029/2020MS002195, 2020.

Bonfils, C. J., Santer, B. D., Fyfe, J. C., Marvel, K., Phillips, T. J., and Zimmerman, S. R.: Human influence on joint changes in temperature, 495 rainfall and continental aridity, Nature Climate Change, 10, 726–731, https://doi.org/10.1038/s41558-020-0821-1, 2020.

Borodina, A., Fischer, E. M., and Knutti, R.: Models are likely to underestimate increase in heavy rainfall in the extratropical regions with high rainfall intensity, Geophysical Research Letters, 44, 7401–7409, https://doi.org/10.1002/2017GL074530, 2017.

Byrne, M. P. and O'Gorman, P. A.: The Response of Precipitation Minus Evapotranspiration to Climate Warming: Why the "Wet-Get-Wetter, Dry-Get-Drier" Scaling Does Not Hold over Land, Journal of Climate, 28, 8078 – 8092, https://doi.org/10.1175/JCLI-D-15-0369.1, 2015.

500 Chen, D., Rojas, M., Samset, B., Cobb, K., Niang, A. D., Edwards, P., Emori, S., Faria, S., Hawkins, E., Hope, P., Huybrechts, P., Meinshausen, M., Mustafa, S., Plattner, G.-K., and Tréguier, A.-M.: Framing, Context, and Methods, book section 1, Cambridge University Press, Cambridge, United Kingdom and New York, NY, USA, https://doi.org/10.1017/9781009157896.004, 2021.

Cowtan, K. and Way, R. G.: Coverage bias in the HadCRUT4 temperature series and its impact on recent temperature trends, Quarterly Journal of the Royal Meteorological Society, 140, 1935–1944, https://doi.org/10.1002/qj.2297, 2014.

505 Dai, A.: Recent Climatology, Variability, and Trends in Global Surface Humidity, Journal of Climate, 19, 3589 – 3606, https://doi.org/10.1175/JCLI3816.1, 01 Aug. 2006.

Deser, C., Phillips, A., Bourdette, V., and Teng, H.: Uncertainty in climate change projections: the role of internal variability, Climate dynamics, 38, 527–546, https://doi.org/10.1007/s00382-010-0977-x, 2012.

Donat, M., Alexander, L., Yang, H., Durre, I., Vose, R., and Caesar, J.: Global Land-Based Datasets for Monitoring Climatic Extremes, 510 Bulletin of the American Meteorological Society, 94, 997 – 1006, https://doi.org/10.1175/BAMS-D-12-00109.1, 2013.

Douville, H., Raghavan, K., Renwick, J., Allan, R. P., Arias, P. A., Barlow, M., Cerezo-Mota, R., Cherchi, A., Gan, T. Y., Gergis, J., Jiang, D., Khan, A., Mba, W. P., Rosenfeld, D., Tierney, J., and Zolina, O.: Water Cycle Changes, book section 8, Cambridge University Press, Cambridge, United Kingdom and New York, NY, USA, https://doi.org/10.1017/9781009157896.010, 2021.

Dunn, R. J. H., Alexander, L. V., Donat, M. G., Zhang, X., Bador, M., Herold, N., Lippmann, T., Allan, R., Aguilar, E., Barry, A. A., Brunet, M., Caesar, J., Chagnaud, G., Cheng, V., Cinco, T., Durre, I., de Guzman, R., Htay, T. M., Wan Ibadullah, W. M., Bin Ibrahim, M. K. I., Khoshkam, M., Kruger, A., Kubota, H., Leng, T. W., Lim, G., Li-Sha, L., Marengo, J., Mbatha, S., McGree, S., Menne, M., de los Milagros Skansi, M., Ngwenya, S., Nkrumah, F., Oonariya, C., Pabon-Caicedo, J. D., Panthou, G., Pham, C., Rahimzadeh, F., Ramos, A., Salgado, E., Salinger, J., Sané, Y., Sopaheluwakan, A., Srivastava, A., Sun, Y., Timbal, B., Trachow, N., Trewin, B., van der Schrier, G., Vazquez-Aguirre, J., Vasquez, R., Villarroel, C., Vincent, L., Vischel, T., Vose, R., and Bin Hj Yussof, M. N.: Development of an Updated Global Land In Situ-Based Data Set of Temperature and Precipitation Extremes: HadEX3, Journal of Geophysical Research: Atmospheres, 125, https://doi.org/10.1029/2019JD032263, 2020.

Eyring, V., Bony, S., Meehl, G. A., Senior, C. A., Stevens, B., Stouffer, R. J., and Taylor, K. E.: Overview of the Coupled Model Intercomparison Project Phase 6 (CMIP6) experimental design and organization, Geoscientific Model Development, 9, 1937–1958, https://doi.org/10.5194/gmd-9-1937-2016, 2016.

Fischer, E. M. and Knutti, R.: Detection of spatially aggregated changes in temperature and precipitation extremes, Geophysical Research Letters, 41, 547–554, https://doi.org/10.1002/2013GL058499, 2014.

Fischer, E. M. and Knutti, R.: Observed heavy precipitation increase confirms theory and early models, Nature Climate Change, 6, 986–991, https://doi.org/10.1038/nclimate3110, 2016.

Fischer, E. M., Sedláček, J., Hawkins, E., and Knutti, R.: Models agree on forced response pattern of precipitation and temperature extremes, Geophysical Research Letters, 41, 8554–8562, https://doi.org/10.1002/2014GL062018, 2014.

Fläschner, D., Mauritsen, T., and Stevens, B.: Understanding the Intermodel Spread in Global-Mean Hydrological Sensitivity, Journal of Climate, 29, 801 – 817, https://doi.org/10.1175/JCLI-D-15-0351.1, 2016.

Friedman, J. H., Hastie, T., and Tibshirani, R.: Regularization Paths for Generalized Linear Models via Coordinate Descent, Journal of Statistical Software, 33, 1–22, https://doi.org/10.18637/jss.v033.i01, 2010.

Giorgi, F., Coppola, E., and Raffaele, F.: A consistent picture of the hydroclimatic response to global warming from multiple indices: Models and observations, Journal of Geophysical Research: Atmospheres, 119, 11,695–11,708, https://doi.org/10.1002/2014JD022238, 2014.

Hawkins, E. and Sutton, R.: Time of emergence of climate signals, Geophysical Research Letters, 39, https://doi.org/10.1029/2011GL050087, 2012.

Hawkins, E., Frame, D., Harrington, L., Joshi, M., King, A., Rojas, M., and Sutton, R.: Observed Emergence of the Climate Change Signal: From the Familiar to the Unknown, Geophysical Research Letters, 47, e2019GL086259, https://doi.org/10.1029/2019GL086259, 2020.

Hegerl, G. C., von Storch, H., Hasselmann, K., Santer, B. D., Cubasch, U., and Jones, P. D.: Detecting Greenhouse-Gas-Induced Climate Change with an Optimal Fingerprint Method, Journal of Climate, 9, 2281 – 2306, https://doi.org/10.1175/1520-0442(1996)009<2281:DGGICC>2.0.CO;2, 1996.

Held, I. M. and Soden, B. J.: Robust Responses of the Hydrological Cycle to Global Warming, Journal of Climate, 19, 5686 – 5699, https://doi.org/10.1175/JCLI3990.1, 2006.

Hoerling, M., Eischeid, J., and Perlwitz, J.: Regional Precipitation Trends: Distinguishing Natural Variability from Anthropogenic Forcing, Journal of Climate, 23, 2131 – 2145, https://doi.org/10.1175/2009JCLI3420.1, 2010.

Kent, C., Chadwick, R., and Rowell, D. P.: Understanding Uncertainties in Future Projections of Seasonal Tropical Precipitation, Journal of Climate, 28, 4390 – 4413, https://doi.org/10.1175/JCLI-D-14-00613.1, 2015.

550 King, A. D., Donat, M. G., Fischer, E. M., Hawkins, E., Alexander, L. V., Karoly, D. J., Dittus, A. J., Lewis, S. C., and Perkins, S. E.: The timing of anthropogenic emergence in simulated climate extremes, Environmental Research Letters, 10, 094 015, https://doi.org/10.1088/1748-9326/10/9/094015, 2015.

Kirchmeier-Young, M. C. and Zhang, X.: Human influence has intensified extreme precipitation in North America, Proceedings of the National Academy of Sciences, 117, 13 308–13 313, https://doi.org/10.1073/pnas.1921628117, 2020.

555 Knutson, T. R. and Zeng, F.: Model Assessment of Observed Precipitation Trends over Land Regions: Detectable Human Influences and Possible Low Bias in Model Trends, Journal of Climate, 31, 4617 – 4637, https://doi.org/10.1175/JCLI-D-17-0672.1, 2018.

Kotz, M., Wenz, L., Lange, S., and Levermann, A.: Changes in mean and extreme precipitation scale universally with global mean temperature across and within climate models, https://doi.org/10.31223/X5C631, 2022.

Li, C., Zwiers, F., Zhang, X., Li, G., Sun, Y., and Wehner, M.: Changes in Annual Extremes of Daily Temperature and Precipitation in CMIP6
560 Models, Journal of Climate, 34, 3441 – 3460, https://doi.org/10.1175/JCLI-D-19-1013.1, 2021.

Madakumbura, G. D., Thackeray, C. W., Norris, J., Goldenson, N., and Hall, A.: Anthropogenic influence on extreme precipitation over global land areas seen in multiple observational datasets, Nature Communications, 12, 3944, https://doi.org/10.1038/s41467-021-24262-x, 2021.

Marvel, K. and Bonfils, C.: Identifying external influences on global precipitation, Proceedings of the National Academy of Sciences, 110, 19 301–19 306, https://doi.org/10.1073/pnas.1314382110, 2013.

565 Mehran, A., AghaKouchak, A., and Phillips, T. J.: Evaluation of CMIP5 continental precipitation simulations relative to satellite-based gauge-adjusted observations, Journal of Geophysical Research: Atmospheres, 119, 1695–1707, https://doi.org/10.1002/2013JD021152, 2014.

Min, S.-K., Zhang, X., Zwiers, F. W., and Hegerl, G. C.: Human contribution to more-intense precipitation extremes, Nature, 470, 378–381, https://doi.org/10.1038/nature09763, 2011.

570 Noake, K., Polson, D., Hegerl, G., and Zhang, X.: Changes in seasonal land precipitation during the latter twentieth-century, Geophysical Research Letters, 39, https://doi.org/10.1029/2011GL050405, 2012.

O'Gorman, P. A. and Schneider, T.: The physical basis for increases in precipitation extremes in simulations of 21st-century climate change, Proceedings of the National Academy of Sciences, 106, 14 773–14 777, https://doi.org/10.1073/pnas.0907610106, 2009.

Paik, S., Min, S.-K., Zhang, X., Donat, M. G., King, A. D., and Sun, Q.: Determining the Anthropogenic Greenhouse Gas
575 Contribution to the Observed Intensification of Extreme Precipitation, Geophysical Research Letters, 47, e2019GL086 875, https://doi.org/10.1029/2019GL086875, 2020.

Pendergrass, A. G.: The Global-Mean Precipitation Response to CO2-Induced Warming in CMIP6 Models, Geophysical Research Letters, 47, e2020GL089 964, https://doi.org/https://doi.org/10.1029/2020GL089964, 2020.

Pendergrass, A. G. and Hartmann, D. L.: The atmospheric energy constraint on global-mean precipitation change, Journal of climate, 27,
580 757–768, https://doi.org/10.1175/JCLI-D-13-00163.1, 2014.

Pendergrass, A. G., Knutti, R., Lehner, F., Deser, C., and Sanderson, B. M.: Precipitation variability increases in a warmer climate, Scientific reports, 7, 1–9, https://doi.org/10.1038/s41598-017-17966-y, 2017.

Pfahl, S. and Wernli, H.: Quantifying the Relevance of Cyclones for Precipitation Extremes, Journal of Climate, 25, 6770 – 6780, https://doi.org/10.1175/JCLI-D-11-00705.1, 2012.

585 Pfahl, S., O'Gorman, P. A., and Fischer, E. M.: Understanding the regional pattern of projected future changes in extreme precipitation, Nature Climate Change, 7, 423–427, https://doi.org/10.1038/nclimate3287, 2017.

Roderick, M. L., Sun, F., Lim, W. H., and Farquhar, G. D.: A general framework for understanding the response of the water cycle to global warming over land and ocean, Hydrology and Earth System Sciences, 18, 1575–1589, https://doi.org/10.5194/hess-18-1575-2014, 2014.

Santer, B. D., Taylor, K. E., Wigley, T. M., Penner, J. E., Jones, P. D., and Cubasch, U.: Towards the detection and attribution of an anthro-
590 pogenic effect on climate, Climate Dynamics, 12, 77–100, https://doi.org/10.1007/BF00223722, 1995.

Schneider, U., Finger, P., Meyer-Christoffer, A., Rustemeier, E., Ziese, M., and Becker, A.: Evaluating the Hydrological Cycle over Land Using the Newly-Corrected Precipitation Climatology from the Global Precipitation Climatology Centre (GPCC), Atmosphere, 8, https://doi.org/10.3390/atmos8030052, 2017.

Simon, N., Friedman, J. H., Hastie, T., and Tibshirani, R.: Regularization Paths for Cox's Proportional Hazards Model via Coordinate
595 Descent, Journal of Statistical Software, 39, 1–13, https://doi.org/10.18637/jss.v039.i05, 2011.

Sippel, S., Meinshausen, N., Fischer, E. M., Székely, E., and Knutti, R.: Climate change now detectable from any single day of weather at global scale, Nature Climate Change, 10, 35–41, https://doi.org/10.1038/s41558-019-0666-7, 2020.

Sun, Q., Zwiers, F., Zhang, X., and Yan, J.: Quantifying the Human Influence on the Intensity of Extreme 1- and 5-Day Precipitation Amounts at Global, Continental, and Regional Scales, Journal of Climate, 35, 195 – 210, https://doi.org/10.1175/JCLI-D-21-0028.1, 2022.

600 Tramblay, Y., Mimeau, L., Neppel, L., Vinet, F., and Sauquet, E.: Detection and attribution of flood trends in Mediterranean basins, Hydrology and Earth System Sciences, 23, 4419–4431, https://doi.org/10.5194/hess-23-4419-2019, 2019.

Wehner, M., Gleckler, P., and Lee, J.: Characterization of long period return values of extreme daily temperature and precipitation in the CMIP6 models: Part 1, model evaluation, Weather and Climate Extremes, 30, 100 283, https://doi.org/10.1016/j.wace.2020.100283, 2020.

Westra, S., Alexander, L. V., and Zwiers, F. W.: Global Increasing Trends in Annual Maximum Daily Precipitation, Journal of Climate, 26,
605 3904 – 3918, https://doi.org/10.1175/JCLI-D-12-00502.1, 2013.

Wu, P., Christidis, N., and Stott, P.: Anthropogenic impact on Earth's hydrological cycle, Nature Climate Change, 3, 807–810, https://doi.org/10.1038/nclimate1932, 2013.

Zhang, X., Wan, H., Zwiers, F. W., Hegerl, G. C., and Min, S.-K.: Attributing intensification of precipitation extremes to human influence, Geophysical Research Letters, 40, 5252–5257, https://doi.org/10.1002/grl.51010, 2013.

610 Zittis, G., Bruggeman, A., and Lelieveld, J.: Revisiting future extreme precipitation trends in the Mediterranean, Weather and Climate Extremes, 34, 100 380, https://doi.org/10.1016/j.wace.2021.100380, 2021.